Acta Astronautica 208 (2023) 194–204

Contents lists available at ScienceDirect

Acta Astronautica

journal homepage: www.elsevier.com/locate/actaastro

Research paper

Design and validation of a dual-band circular polarization patch antenna and stripline combiner for the FSSCat mission☆

Lara Fernandez [a,b,d,*], Joan Francesc Munoz-Martin [a,f], Joan A. Ruiz-de-Azua [c], Anna Calveras [b], Adriano Camps [a,d,e]

[a] "CommSensLab", Department of Signal Theory and Communications - UPC BarcelonaTech, Spain
[b] Department of Network Engineering - UPC BarcelonaTech, Spain
[c] i2Cat Foundation Space Communications Research Group, Spain
[d] Institute of Space Studies of Catalonia (IEEC) - Space Science and Technology Research Group, CTE/UPC, Spain
[e] United Arab Emirates (UAE) University[1], Al Ain, Abu Dhabi, United Arab Emirates
[f] California Institute of Technology/Jet Propulsion Laboratory, United States of America

ARTICLE INFO

Keywords:
CubeSat
Nanosatellite
Patch
Antenna
L-band
Earth Observation

ABSTRACT

The FMPL-2 payload on board the [3]Cat-5/A 6 Unit CubeSat, part of the FSSCat CubeSat mission, includes a dual L-Band Microwave Radiometer and a Global Navigation Satellite System Reflectometer, in one instrument, implemented in a Software Defined Radio. One of the design challenges of this payload was its Nadir looking Antenna, which had to be directive (> 12 dB), dual-band at 1400–1427 MHz and 1575.42 MHz, left-hand circularly polarized, and with important envelope restrictions, notably with a low profile. After a trade-off analysis, the best design solution appeared to be an array of six elements each of them being a stacked dual-band patch antenna, with diagonal feed to create the circular polarization, and a six to one stripline combiner. The design process of the elementary antennas first includes a theoretical analysis, to obtain the approximate dimensions. Then, by means of numerical simulations, prototyping, and adjusting the results in the simulations, the manufacturing errors and dielectric constant tolerances, to which patch antennas are very sensitive, can be characterized. A similar approach is taken with the combiner. This article includes the theoretical analysis, simulations, and prototype results, including the Flight Model assembly and characterization.

1. Introduction

The appearance of the CubeSat standard [1] in 1999 led to a change of paradigm in the space sector, and somehow triggered the so-called New Space. This standard defines the satellites envelope and weight, classified by Units (U). Being a 1U satellite a 10 cm side cube, and a 6U a combination of 3 × 2 U's. Also, the weight per U was initially fixed to 1.3 kg, but in the CubeSat Design Specification rev. 14 (July 2020) [2] the requirement has been relaxed up to 2 kg of mass per U. This standard has boosted the technology development of Commercial-off-the-Shelf (COTS) avionics, allowing a cost reduction in the development, and also the launch due to the standardization of the interfaces with the launch vehicle, and the reduced weight.

Initially, Universities and other small entities were the ones taking advantage to launch their own satellites. However, in the past decade space agencies and numerous companies have launched or participated in CubeSat or smallsat missions, following the so-called New Space trend. For instance, NASA has launched IceCube [3] a 3U CubeSat that generates cloud ice maps and RainCube [4] that contains a Ka-band Radar and a deployable parabolic antenna in a 6U CubeSat.

Among the Earth Observation (EO) payloads for CubeSats or small satellites, due to power limitations, passive ones e.g. optical imagers, Global Navigation Satellite System Radio Occultations (GNSS-RO), or those that make use of Global Navigation Satellite System Reflectometry (GNSS-R) are gaining momentum. In the latter, the spatial resolution does not depend on the antenna size, and allows to perform

☆ This work was by the Programa Estatal para Impulsar la Investigación Científico-Técnica y su Transferencia, del Plan Estatal de Investigación Científica, Técnica y de Innovación 2021-2023 (Spain) and in part by the European Social Fund (ESF). It is also funded in part by the Secretaria d'Universitats i Recerca del Departament d'Empresa i Coneixement de la Generalitat de Catalunya 2017 SGR 376 and 2017 SGR 219. This work has also been founded by the grant PID2019-106808RA-I00 funded by MCIN/AEI/10.13039/501100011033. Finally, this research was possible thanks to the FI-2019 grant from AGAUR-Generalitat de Catalunya, Spain.

* Corresponding author at: "CommSensLab", Department of Signal Theory and Communications - UPC BarcelonaTech, Spain.
E-mail address: lara.fernandez.c@upc.edu (L. Fernandez).

[1] Visiting professor.

https://doi.org/10.1016/j.actaastro.2023.03.042
Received 10 October 2022; Received in revised form 16 February 2023; Accepted 29 March 2023
Available online 1 April 2023

Fig. 1. FSSCat satellites render (credit: UPC).

ocean monitoring [5], obtain soil moisture [6], and detect flooded regions [7] or ice cover [8]. This technique has been validated in missions such as the UK-DMC [9], the UK TechnoDemoSat-1 (TDS-1) [10], and the CYGNSS constellation from NASA [11].

Additionally, combining GNSS-R with L-Band Microwave Radiometry (MWR) [12,13] measurements improves the spatial resolution and accuracy of soil moisture and ocean salinity products [14]. This was done in the FSSCat mission [15] a mission composed by two 6U CubeSats, ^{3}Cat-5/A and ^{3}Cat-5/B (Fig. 1), winner of the Copernicus Masters ESA Sentinel Small Satellite $\mathcal{S}^3$ Challenge [16] and launched on September the 3rd 2020.

^{3}Cat-5/A main payload is the Flexible Microwave Payload 2 (FMPL-2) [17] that combines a GNSS-R and a MWR in the same instrument. It is based on the PAU concept [18] and it inherits from the PYCARO on ^{3}Cat-2 [19] launched in 2016 (GNSS-R instrument), and the FMPL-1 on ^{3}Cat-4 [20], which consists of a MWR with radio interference mitigation, and a GNSS-R based on an RTL Software Defined Radio (RTL-SDR) device.

^{3}Cat-5/B main payload is a hyperspectral camera, the Hyperscout 2, [21] working in the Visible and Near InfraRed (VNIR) bands, and Thermal InfraRed (TIR) band. It also features an Artificial Intelligence (AI) processor for cloud detection, to optimize the data download and transmit only useful images. Moreover, both satellites are equipped with an optical inter-satellite from Golbriak Space OÜ (Estonia), and a Ultra-High Frequency (UHF) inter-satellite link developed in-house.

Overall, one of the main objectives of the mission is to provide full coverage of both the North and South poles providing Sea Ice Concentration and Sea Ice Thickness products [22,23] from the data acquired with the FMPL-2. To achieve that, it was necessary to manufacture a custom antenna that resonates at both the MWR (1400–1427 MHz) and Global Positioning System (GPS) L1/Galileo E1 (1575,42 MHz) band for GNSS-R, with a Directivity (D) larger than 12 dB at both bands. It is also a requirement to have Left Hand Circular Polarization (LHCP), especially in the L1/E1 band, and smaller Return Losses (RL) than −10 dB at 1413 MHz and −5 dB at 1575,42 MHz.

The dimensions and mass of the antenna are also critical since the antenna is allocated in one of the outer faces of the spacecraft, which constrains it from fitting within the CubeSat envelope. Moreover, the adverse conditions experienced during launch in terms of structural damage to the components and the extreme temperature changes experienced when in orbit also have to be considered in the design, taking into account that the antenna is pointing to nadir.

This work presents the design, implementation, and testing of the nadir antenna for the FMPL-2, including the results of the Flight Model (FM) flying onboard the ^{3}Cat-5/A spacecraft. The design first comprises the requirements definition. Then, a survey of the different design solutions is done, and the optimum one is selected. After that, simulations of the antenna dimensions are performed, and a prototype of each one is manufactured to verify the simulation model. Finally, the results of the FM and the environmental testing campaign are presented.

This article is organized as follows: Section 2 lists the nadir antenna requirements. Section 3 contains the theoretical analysis and simulations of the design. Section 4 presents the design and performance of the prototypes, and the nadir antenna FM. Finally, Section 5 presents the conclusions of this work.

Table 1
Requirements definition for the nadir antenna.

ID	Requirement description
001	The nadir antenna shall work with a minimum directivity of 12 dBi at 1575.42 MHz
002	The nadir antenna shall work with a minimum directivity of 12 dBi in the 1400–1427 MHz band
003	The nadir antenna shall receive in Left Hand Circular Polarization with an axial ratio smaller than 3 between 1400–1427 MHz and at 1575.42 MHz
004	The nadir antenna shall have return losses smaller than 10 dB in the 1400–1427 MHz band
005	The nadir antenna shall have return losses smaller than 5 dB of return losses at 1575.42 MHz
006	The nadir antenna shall have a maximum envelope of 300 mm × 200 mm × 7 mm with a single SMA interface connector
007	The nadir antenna shall be able to withstand vacuum and temperatures between 80 °C and −20 °C

2. Nadir antenna requirements definition

The requirements stated for the nadir antenna mentioned along Section 1, are summarized in Table 1. The Directivity (D) and Return Losses (RL) requirements have been set by the Payload Engineer, and the envelope requirements of the platform provider, according to the interface and the structural analysis.

First, it is required to select the best antenna type for the particular use case. In [24], a survey of antennas onboard CubeSats is done, and among all the design solutions presented, the helical and patch antennas are the ones that could comply with the requirements. Helical antennas offer circular polarization, high directivity, and are broadband. These are stowed during launch and deployed in orbit. There are some solutions for industrial helical antennas with flight heritage, such as the ones embarked in the GOMX-1 [25] and GOMX-3 [26] for Automatic Dependent Surveillance–Broadcast (ADS-B) applications. Furthermore, a Nanoavionics spacecraft carrying an Internet of Things (IoT) payload with a helical antenna was also launched by Lacuna Space [27]. Also, a quadrifilar helical antenna [28] that takes up half of a CubeSat unit has a commercially available option. Furthermore, there are tailored solutions such as the one created for the ^{3}Cat-4 mission [29,30]. However, all these antennas are not compliant with the envelope requirements, since they require space on the internal stack of the satellite.

As seen in TechDemoSat-1 [10], ^{3}Cat-2 [31], and CyGNSS [11] an array of patch antennas mounted on the outer side of the satellite provides enough directivity for spaceborne GNSS-R payloads. Other solutions consider different types of materials for transmission line type antennas [32,33], although these perform similarly to standard patch antennas. With the directivity required for the nadir antenna, an array of 6 patches requires a 6U face to distribute the antennas. This design solution aligns with the envelope restriction given for the antenna. However, having six different antenna elements requires to have a combiner that combines the signals into one, to have a single output in an SubMiniature version A (SMA) port. An in-depth analysis of the antenna and combiner design is presented in Section 3, where the dual-band matching and the type of combiner solutions are addressed.

3. Materials and methods

This section includes first an overview of the design. Then, a theoretical background on circular polarization and dual frequency band patch antennas, and the simulations of the prototypes manufactured. Finally, the theoretical background and the simulations of the combiner are presented.

3.1. Nadir antenna design

To provide a better understanding of some of the design constraints, the final nadir antenna design is first presented, as it can be better understood. Aside from the envelope dimensions, the platform provider also fixed some M2.5 clearance holes to integrate it in the platform. Due to the dimensions of the antenna, and the position of the mechanical interface holes the six radiating elements can be placed in a 3 by 2 distribution, as seen in Fig. 2.

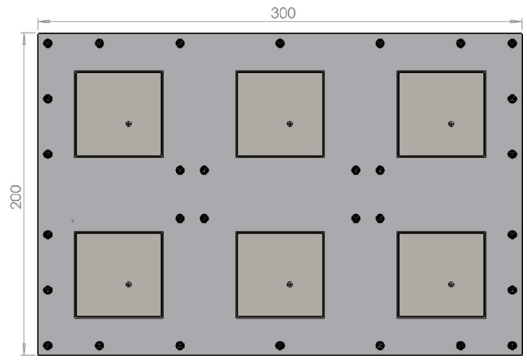

Fig. 2. Nadir antenna dimensions.

The design solution that complies with the requirements has been to stack four printed circuit boards (PCBs). As seen in Fig. 3, the top one contains the six GPS L1 patches, below there is another one with six more patches for the MWR, and a ground plane on the bottom layer for the antennas. Finally, the two PCBs at the bottom have ground planes on either side, and the stripline combiner in the center.

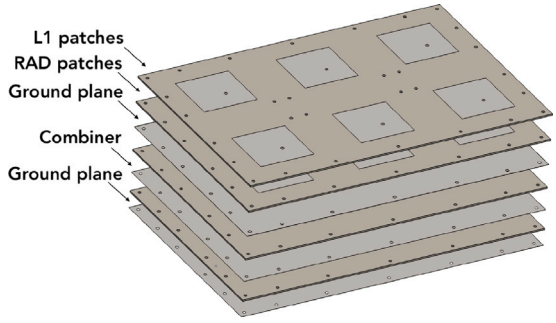

Fig. 3. Extruded view of the nadir antenna.

3.2. Antenna design: Theoretical background

Patch or microstrip antennas [34], are formed by a dielectric substrate, with dielectric constant ϵ_r, with a ground plane on one side of the substrate, and the radiating element on the other side. The dielectric constant ϵ_r defines the size of the antenna, but also the losses. For higher constants, the antennas are smaller, but losses are typically higher too.

There are several feeding methods for patch antennas, shown in Fig. 4. The four most common feeding methods are microstrip feed, coaxial feed, aperture feed, and slot feed. The microstrip and coaxial feeds are the easiest to manufacture and match. The coaxial feed has a narrower bandwidth as compared to a microstrip feed.

The proximity coupled feed consists of a stack of two layers of substrate: the radiating element is placed on the top, a microstrip line feeding the antenna in the middle, and in the bottom the ground plane of the antenna. So, the feed line is coupled with the radiating element.

The aperture coupled feed has also two substrate layers, the radiating element in the top layer, a ground plane with a slot in the middle layer, and at the bottom a microstrip line. In this case, the microstrip line is the antenna feed, which couples with the radiating element through the slot.

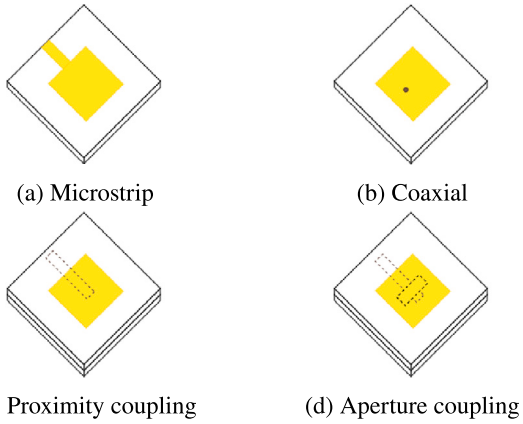

Fig. 4. Patch antenna feeding methods.

These two feeding methods are harder to manufacture and to match, than the previous two methods, but ensure less spurious radiation.

Depending on the feeding method used, the patch antenna can have linear or circular polarization. In order two achieve circular polarization there has to be a 90° phase shift between the two main modes of the antenna. Moreover, a configuration of the phase shifts the polarization can be either Right Hand Circular Polarization (RHCP) or LHCP.

If the feeding method is a microstrip line (Fig. 5) the circular polarization can be obtained by feeding two different sides of the antenna with a 90° phase shift. This would be the case for the (a) $\lambda/4$ power splitter, or the (b) 90° hybrid. Another technique is to feed the antenna on only one side and place a slot in the center with a diagonal orientation. In all these cases the radiating element has a square shape.

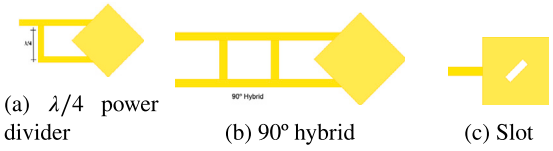

Fig. 5. Circular polarization configuration with microstrip line feed.

The dimensions of the square antenna are computed as shown in Eq. (1) [34], where c_0 is the speed of light, f_0 the central frequency, and ϵ_r the dielectric constant of the material.

$$W = \frac{c_0}{2 \cdot f_0} \cdot \sqrt{\frac{2}{\epsilon_r + 1}} \tag{1}$$

If circular polarization has to be achieved with a coaxial feed (Fig. 6), the antenna can be fed in the diagonal, or in the center of one edge, but with slant corners. For these configurations, the antennas are slightly rectangular. The diagonal feed has right hand circular polarization if the feed is placed in the upwards right diagonal, and LHCP if it is placed in the upwards left one.

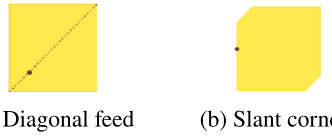

Fig. 6. Circular polarization configuration with coaxial feed.

In these cases, an adjustment on the width (W) of the patches is performed considering the 90° phase shift. To compute this, the frequencies at which the imaginary part of the load are −45° and 45°

have to be computed. Thus, if the antenna is designed at $f_{0°}$, where $Im(Z) = 0°$, the frequencies $f_{-45°}$ and $f_{45°}$, where the $Im(Z) = -45°$ and $Im(Z) = 45°$ have to be found.

The adjustment in the width and length of the antennas is computed as shown in Eq. (2) [34], where W is the width of a square patch antenna.

$$W_x = W \cdot \frac{f_0}{f_{-45°}}; W_y = W \cdot \frac{f_0}{f_{45°}} \tag{2}$$

These feed configurations to obtain circular polarization only resonate at one frequency. According to [35] dual-band patch antennas can be achieved through three different techniques (1) orthogonal mode [36–38], (2) multi-patch [39], and (3) reactively loaded.

The orthogonal mode is based on the idea that a single or two feeding points are matched at the same time at two frequencies. This can be achieved by feeding the antenna either with a coaxial or slot coupling.

The multi-patch consists of either stacking multiple radiating elements or placing them on the co-planar surface of the same antenna. If the elements are stacked, the feed and matching can be performed either by employing a coaxial feed or a slot. If they are placed on a co-planar surface, they can be obtained with parallel rectangular dipoles or a cross-subarray with a larger cross-shaped element in the center, and four smaller squares on the sides. The cross-subarray is tailored to designs that have a large separation between frequencies.

The third method consists of using reactive loads to match the patches. For this reason, stubs, notches, capacitors, or slots are added to the patches.

For the nadir antenna design, a coaxial feed is the best option, since it allows connecting directly the antennas to the combiner within the stack of PCBs. Also, it is necessary to have a single feeding point for each of the antennas, since the output of the nadir antenna has to be a single SMA connector and not one per band. Thus, the selected design is the multi-patch configuration with coaxial diagonal feed.

3.3. Antenna design: Simulations

Numerical simulations using CST Studio Suite have been conducted to fine-tune the design and make it compliant with the requirements. To achieve the antenna matching at the frequencies, an iterative approach of simulating, prototyping, and adjusting the simulations based on the results obtained has been followed, because simulations never account for all system imperfections and tolerances.

Moreover, these types of antennas are very sensitive to the dimensions of the radiating element, and the dielectric constant of the material. So, in the iterative process two aspects are characterized: (1) the effect of the manufacturing tolerances in the antenna, and (2) the difference between the ϵ_r in the simulations, and the prototypes.

The design is first performed for a single 100 × 100 mm^2 patch antenna This antenna is a stack of two elements with a diagonal coaxial feed. The dual-frequency band is achieved by utilizing the antenna stack, and the LHCP with the diagonal feed, which is placed on the upwards left diagonal. The dielectric material used is Rogers 4003C, the thickness of the material is 1.524 mm and the theoretical dielectric constant is $\epsilon_r = 3.18$.

To simulate the antenna a model is defined with the parameters listed in Table 2. The dimensions of the ground plane, GPX, and GPY, are 100 × 100 mm^2. The dimensions for the patches and the position of the coaxial feed are chosen based on the simulations.

3.3.1. Single-frequency patch antenna

The theoretical width of the antennas can be seen in Table 3. These theoretical widths are the starting point to design two single-frequency antennas. One antenna will be matched at the MWR band and the other one at GPS L1.

The first step in the design of these two square antennas is to perform a parameter sweep of CoaxPosX to find the position of the coaxial

Table 2
Single patch antenna simulation variables.

Name	Description
GPX	Ground plane dimension in X axis
GPY	Ground plane dimension in y axis
RADX	Radiometer patch dimension in x axis
RADY	Radiometer patch dimension in y axis
L1X	GPS L1 patch dimension in x axis
L1Y	GPS L1 patch dimension in y axis
CoaxPosX	Position of the coaxial connector in the X axis
CoaxPosY	Position of the coaxial connector in the Y axis

Table 3
Patch antennas theoretical dimensions.

f (MHz)	Width (mm)
1413	$W = \frac{3 \cdot 10^8}{2 \cdot 1413 \cdot 10^3} \cdot \sqrt{\frac{2}{3.55+1}} = 70.3$
1575.42	$W = \frac{3 \cdot 10^8}{2 \cdot 1575.42 \cdot 10^3} \cdot \sqrt{\frac{2}{3.55+1}} = 63.1$

Table 4
Patches dimensions with 90° phase-shift.

f_0 (MHz)	$f_{-45°}$; $f_{45°}$ (MHz)	$Width_x$ (mm)	$Width_y$ (mm)
1439.3	1445.8; 1435.0	$W \cdot 0.9955$	$W \cdot 1.0029$
1590.2	1597.9; 1584.9	$W \cdot 0.9951$	$W \cdot 1.0033$

Table 5
Results for single-frequency with circular polarization antenna simulations.

f (MHz)	S11 (dB)	AR (dB)
1413	−11.7	1.5
1575	−7.1	2.3

that has the lowest RL. The calculations and simulations are performed at the center frequency of each frequency band. The simulations are matched at higher frequencies than the theoretical ones, since at this point the error in center frequency between the simulations and the real prototypes was already characterized.

Once the RL is the minimum possible the frequencies for which the imaginary part of the impedance of the antenna is −45° and 45° are obtained, to ensure a circular polarization (i.e. 90° phase shift between the two modes). Results can be seen in Table 4. With the difference between the two frequencies, the coefficients to adjust the width in the X and Y direction of the antenna are obtained.

3.3.2. Single-frequency circular polarization patch antenna

Considering these adjustments in the width of the antennas two single-frequency circular-polarization antennas are simulated. The results obtained from these antennas are shown in Table 5.

These two antennas have been prototyped and measured in the UPC Antenna Lab Anechoic Chamber [40]. The results for these measures are presented in Section 4.

3.3.3. Dual-frequency circular polarization antenna stack

After designing the single-frequency circularly polarized antennas, the design of the stack with double-frequency and circular polarization is performed (see Fig. 7).

The design of the dual-frequency antenna is performed by stacking two patch antennas. Thus, the coupling between both antennas resonates at the two desired frequencies. The design of these antennas has consisted of doing combinations of parameter sweeps between the width of the MWR patch and the GPS L1 patch. The final dimensions for this antenna can be seen in Table 6.

The S11 parameter for the stack antenna are illustrated in Fig. 8. The matching frequencies in the simulation are higher than the desired ones since a frequency shift between the simulation and the prototype has been characterized based on previous prototypes manufactured.

Table 6
Results for the final design of the antenna stack simulations.

GPX	100 mm	RADX	53.909 mm
GPY	100 mm	RADY	54.801 mm
L1X	51.963 mm	CoaxPosX	−6.110 mm
L1Y	52.835 mm	CoaxPosY	6.010 mm

Table 7
Directivity of six elements antenna array simulations.

Real f (MHz)	Simulation f (MHz)	D (dB)
1413	1520.5	13.4
1575.42	1599.6	13.8

This difference depends on the specific dielectric used and the matching frequency, and it is due to the modeling errors of the dielectric, and the manufacturing tolerances. Thus, this phenomenon has to be characterized for every specific scenario.

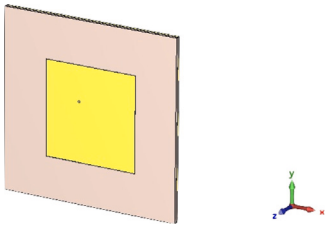

Fig. 7. Dual-frequency with circular polarization stack antenna.

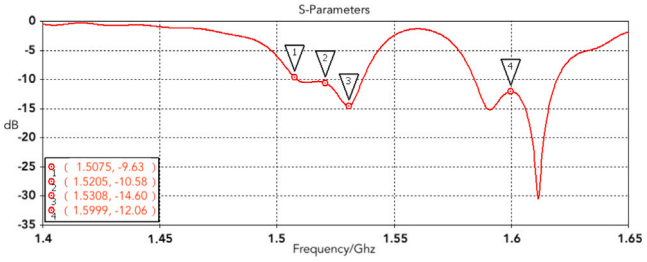

Fig. 8. S11 parameters for single antenna simulations.

The Axial Ratio (AR) for this configuration can be seen in Fig. 9. Comparing the AR with the S11 parameter it can be seen that the frequencies at which the antenna is matched are the ones with lower AR.

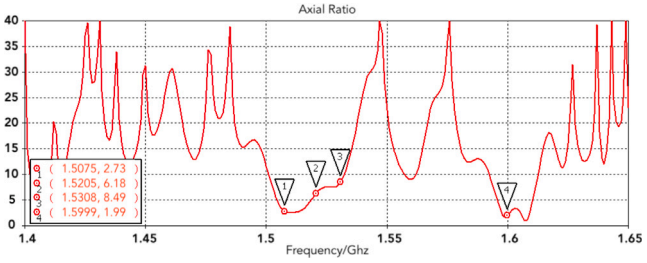

Fig. 9. Axial ratio for single antenna simulations.

Additionally, the antenna is simulated conforming to a 6-patch array. The D for the six-element array positions in a 3 × 2 topology can be found in Table 7. Also, both cuts of the radiation pattern for both frequencies are shown in Figs. 10 and 11.

3.4. Combiner design: Theoretical background

Given that the MWR measures the noise power, i.e. obtains the antenna temperature, no resistive elements can be used in the front-end

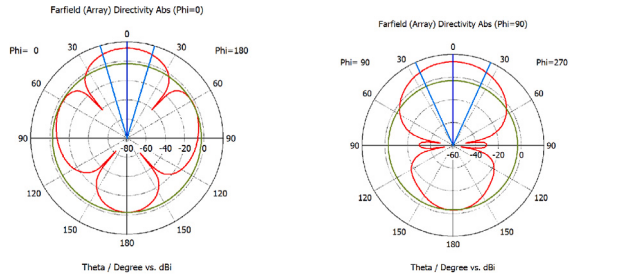

(a) Two elements face ($\varphi = 0$) (b) Three elements face ($\varphi = 90$)

Fig. 10. Radiation patterns of the six elements array simulations at 1413 MHz.

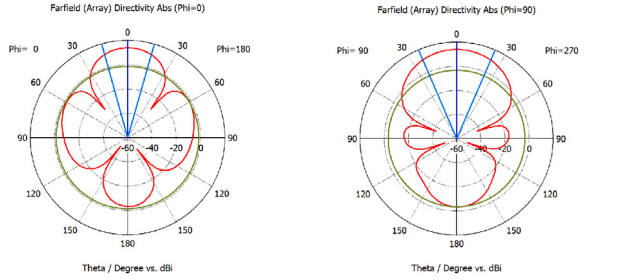

(a) Two elements face ($\varphi = 0$) (b) Three elements face ($\varphi = 90$)

Fig. 11. Radiation patterns of the six elements array simulations at 1575.42 MHz.

chain. For that reason, the combiner is a T-junction. Also, to prevent possible couplings between transmission lines the combiner is done using stripline technology.

Considering the positions of the antenna feeds in the PCB, and the limited space for the combiner, the signal is first combined from the 3 antennas, and then the two outputs obtained are combined into one. This means that two combiners (3:1 and 2:1) have to be designed.

The 3:1 combiner, is shown in Fig. 12(a). It has an input impedance Z_0, and an output impedance Z_1. The relationship between the input and output impedances can be calculated as:

$$Z_1 = \frac{Z_0}{3}. \tag{3}$$

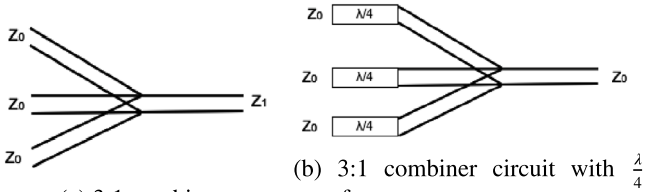

(a) 3:1 combiner (b) 3:1 combiner circuit with $\frac{\lambda}{4}$ transformers

Fig. 12. 3:1 combiner schematics.

If the input impedance is $Z_0 = 50\ \Omega$, the output would be $Z_1 = 16.7\ \Omega$. Between the antenna feeds and the combiner $\frac{\lambda}{4}$ transmission lines are added to match them to $Z_1 = 50\ \Omega$. Thus, the resulting circuit would be as shown in Fig. 12(b).

Based on that premise the reference impedance of the line:

$$Z_0' = \sqrt{Z_0 \cdot Z_1} = \sqrt{50\ \Omega \cdot 3 \cdot 50\ \Omega} = 86.6\ \Omega. \tag{4}$$

In the case of the two-port combiner the same approach is followed. So, the impedance of the line is:

$$Z_1' = \sqrt{Z_0 \cdot Z_2} = \sqrt{50\ \Omega \cdot 2 \cdot 50\ \Omega} = 70.71\ \Omega. \tag{5}$$

The final configuration of the combiner is shown in Fig. 13. The theoretical values for the widths and lengths of the transmission lines can

Table 8
Transmission lines width and length.

W_1	0.94 mm	L_1	53.00 mm
W_2	0.10 mm	W_3	3.10 mm
W_4	1.60 mm		

Table 9
Transmission lines measurements.

W_1	1.00 mm	L_1	53.00 mm
W_2	0.20 mm	W_3	1.30 mm
W_4	0.50 mm		

be found in Table 8. These values have been calculated for a stripline transmission line, the frequency used to calculate the wavelength is 1413 MHz.

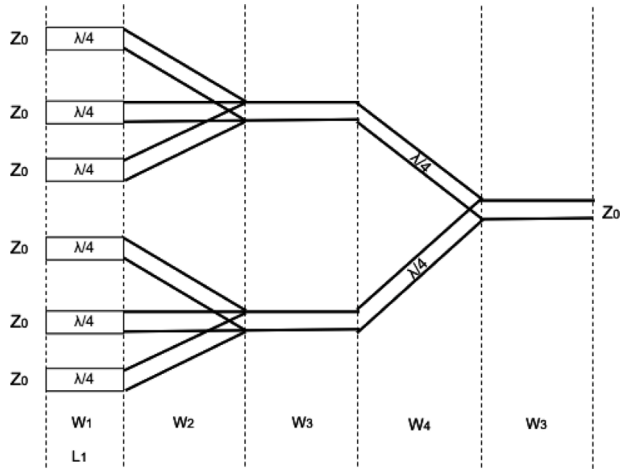

Fig. 13. Final 6:1 combiner configuration.

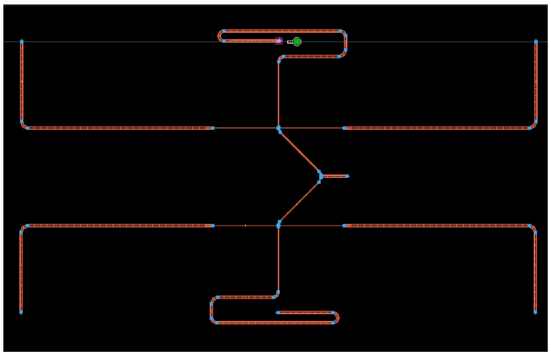

Fig. 14. Combiner layout in ADS.

3.5. Combiner design: Simulations

To match the combiner, the length and width of the lines obtained with theoretical calculus have been inserted in Advanced Design System (ADS) software and adjusted. The simulations have been conducted using the Momentum Tool, which allows configuring the dielectric substrates used, and the ground planes positions.

First, the layout was designed as seen in Fig. 14. Then, the widths of the transmission lines were adjusted to match the combiner. The results obtained from the Momentum simulations are summarized in Table 10, and the measurements for the different transmission lines in Table 9.

Table 10
Simulations of the S parameters of the combiner.

f (MHz)	S parameters (dB)						
	S11	S12	S13	S14	S15	S16	S17
1400	−17.8	−8.0	−8.1	−8.3	−8.0	−8.2	−7.9
1413	−18.1	−8.0	−8.1	−8.3	−8.0	−8.2	−7.9
1427	−17.8	−8.1	−8.1	−8.3	−8.0	−8.2	−8.0
1576	−9.2	−8.3	−8.6	−8.7	−8.7	−8.4	−8.8

Table 11
Measured results for single-frequency circular polarization antenna prototypes.

f (MHz)	S11 (dB)	AR (dB)
1400	−5.2	3.1
1413	−11.7	1.9
1427	−11.8	3.2
1575.42	−11.6	1.6

Table 12
Measured characterization of the dual-frequency circular polarization prototype.

f (MHz)	S11 (dB)
1400	−17.5
1413	−5.7
1427	−1.5
1575.42	−7.3

4. Measured results

This section includes the measured results for the different antenna prototypes and the combiner characterization are presented here. Then, the results of the FM are presented, including a radiofrequency characterization, and a Thermal Vacuum Chamber (TVAC) Test Campaign.

4.1. Antenna characterization

The results for the two antenna prototypes. The prototypes are two single-frequency LHCP antenna, one for the MWR and the other for the GNSS-R. The second prototype is a stack of two patches, this is a single element of the 6-element patch array that is going to conform to the FM.

4.1.1. Single-frequency antenna prototypes

The results for these single-frequency prototypes are in agreement to the simulations. These prototypes have been also measured in the UPC Antenna Lab Anechoic Chamber [40], to verify the simulation model used. As it can be seen in Table 11, the results are satisfactory, since both the matching and the AR are compliant with the requirements. Comparing these results with the simulation (Table 5), and given that the antennas are matched at the correct frequency, it also serves the purpose of verifying the model.

4.1.2. Dual-frequency single stack prototype

This stack antenna prototype conforms a single antenna of the expected FM design, which will have a total of six elements. The prototype of the antenna is shown in Fig. 15.

The results for this antenna can be seen in Table 12. Comparing these results with the simulations, it can be noticed that there is a drift in the frequencies, which was already characterized and identified with the single-frequency antennas.

This antenna complies with the requirements, in terms of RL in some part of the MWR band, and in GPS L1 at the specific frequency. The AR was not measured, since the simulation model was already verified for the single stack (see Fig. 16).

Table 13
Combiner prototype S parameters measured results.

f	S parameters (dB)					
	S12	S13	S14	S15	S16	S17
1400	−5.6	−7.7	−8.1	−5.9	−9.0	−7.7
1413	−8.6	−10.6	−12.8	−9.8	−15.1	−10.1
1427	−12.4	−14.0	−19.8	−15.0	−24.9	−13.8
1575.42	−7.8	−7.4	−6.4	−5.4	−5.7	−7.1

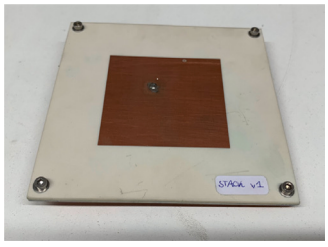

Fig. 15. Stack prototype.

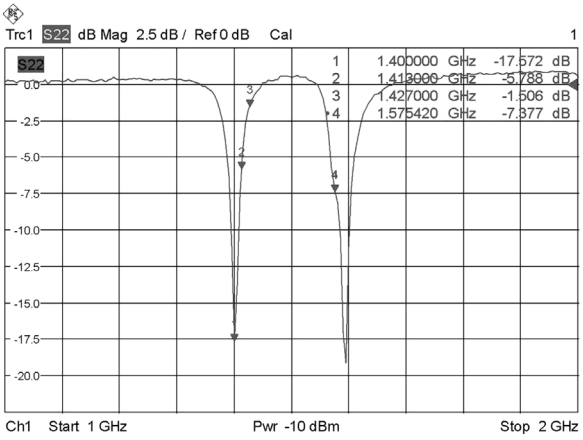

Fig. 16. S11 parameters for the dual-frequency single stack antenna.

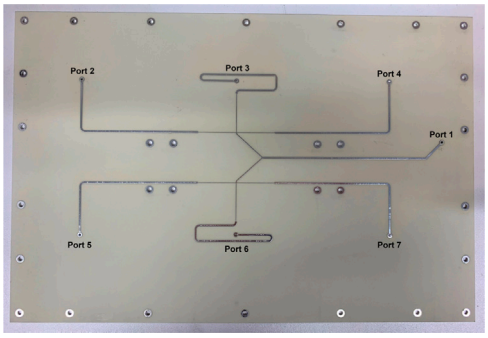

Fig. 17. Combiner QM prototype before assembly.

4.2. Combiner characterization

The combiner was directly manufactured as a whole since it was the only representative manner of having a valid characterization. The scope was to manufacture a Qualification Model (QM) and an FM so that QM could be used to measure and characterize individually.

The combiner was measured with a Vector Network Analyzer (VNA). In Fig. 17 the different ports are defined. Port 1 is the output of the combiner and ports 2 to 7 are the inputs for each one of the

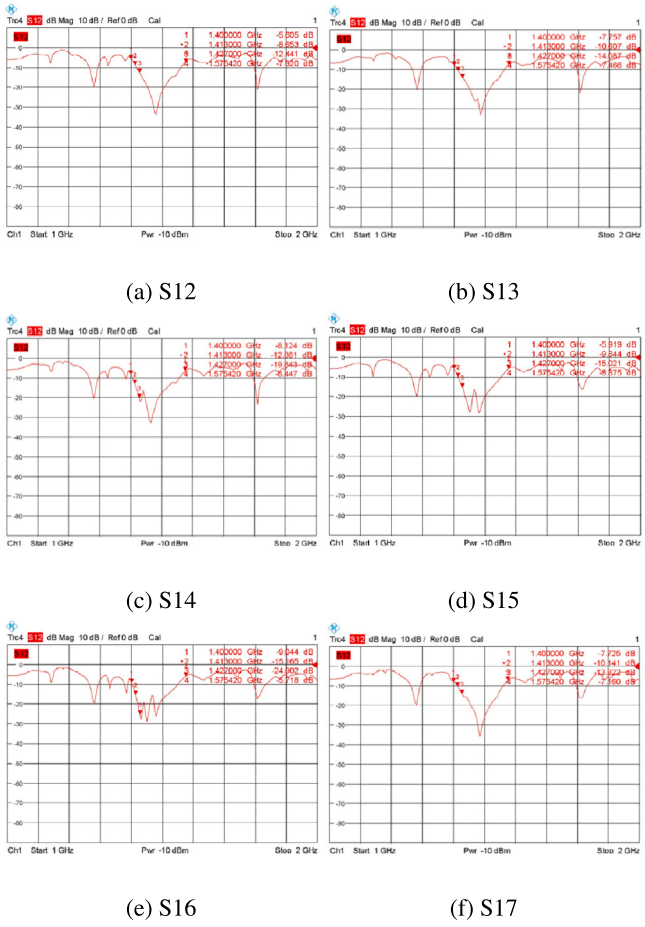

Fig. 18. Combiner S parameters measured results.

patches. The isolation values are summarized in Table 13. Additionally, the images of the measured S parameters can be seen in Fig. 18.

As it can be seen, there are significant differences between the simulations and the real measurements. Also, the different input parameters also show inconsistencies. This is mainly due to the M2.5 interface holes, since some are closer than other to some of the transmission lines. However, this issue is unavoidable given that the interface holes were set by the structural analysis and are required.

4.3. Nadir antenna flight model

The nadir antenna FM is an assembly of a replica of the combiner characterized, the QM, in Section 4.2 and a six patch array of the single antenna prototype characterized in Section 4.1.2.

4.3.1. Assembly and testing sequence

Having simulated, prototyped, and measured both the single antenna and the combiner, the nadir antenna FM can be finally assembled and tested. The assembly and testing process is summarized in Fig. 19.

The first step is to perform the antenna assembly. This comprises mounting the four PCBs together, soldering the feeding points, and keeping all the interface screws bolted at the proper torque, to ensure even spacing between the PCBs.

After performing this process the antenna had the resonance for the L1 band at a higher frequency, so it was reassembled introducing a small air gap between the MWR and the L1 patches. This difference in the matching is probably caused because by a difference in the ϵ_r of the material since the prototypes were manufactured in-house with the same panel but the FM was outsourced.

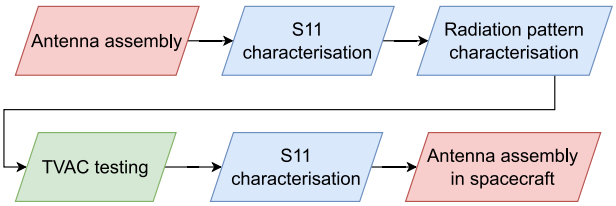

Fig. 19. Assembly and testing procedure of the nadir antenna FM.

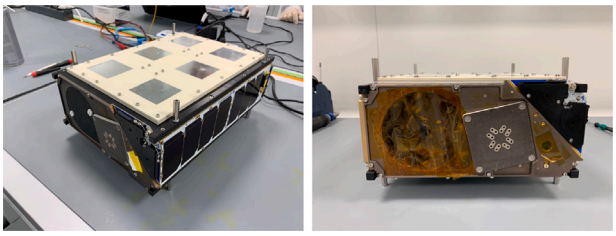

Fig. 20. Nadir antenna integrated in $^3Cat-5/A$ spacecraft.

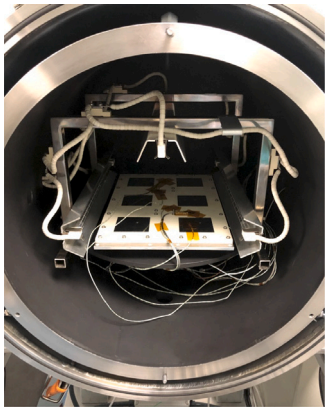

Fig. 21. Nadir antenna FM installed inside the TVAC.

The following steps are characterizing the S11 parameter and performing a TVAC test, to ensure that the antenna is capable of withstanding space conditions (i.e. thermal stress the antenna in vacuum). After TVAC, the S11 parameter has to be characterized again to assess if the TVAC conditions have affected the performance of the antenna. At this point, the radiation pattern is also measured.

Generally, it is good practice to execute the vibration testing first, and then the TVAC testing, following the "test as you fly" philosophy. However, in the case of the nadir antenna, vibration testing was skipped, since it was performed at system level with the whole spacecraft. Although a TVAC test is also done at system level, it was considered necessary to test at subsystem since the antenna is placed on an external surface of the satellite, and at subsystem level it was possible to test under more severe conditions.

Once all the tests were finished, the antenna was assembled into the spacecraft. The images of the antenna integrated into the spacecraft can be seen in Fig. 20.

4.3.2. Thermal vacuum chamber tests of the flight model

The TVAC test was performed in the UPC NanoSat Lab TVAC [41]. This test consisted on placing the antenna, as shown in Fig. 21 in the TVAC, and performing thermal cyclings in vacuum conditions.

The thermal profile used for the test consists of two thermal cyclings with 80° in the hot plateau and −20° in the cold plateau. The profile setup ensures that the antenna is stable for two hours at these temperatures.

Table 14
Directivity, S11 and axial ratio measured results for the nadir antenna.

f (MHz)	D (dB)	G (dB)	S11 (dB)	AR (dB)
1413	12.1	10.1	−8.3	0.5
1575.42	10.2	5.48	−6.8	6.3

The measurements of the temperature once the TVAC is depressurized are performed with thermocouples. The temperature retrievals from the thermocouples can be seen in Fig. 22. All thermocouples were placed on the top and bottom parts of the antenna, except for the red one, which is connected to the TVAC shroud. This shroud is filled with Liquid Nitrogen (LN2), when the cold plateau is performed, to cool the chamber.

After the thermal cyclings are performed, the TVAC is pressurized and a measurement of the S11 parameter and the radiation pattern are performed again.

4.3.3. Radiofrequency characterization

The antenna was characterized by measuring the S11 parameter measurement with a VNA and the radiation pattern, gain (G) and AR measurements in the UPC Antenna Lab Anechoic Chamber. The results for these tests are shown in Table 14. Additionally, in Fig. 23 the S11 parameters can be seen, and in Figs. 24 and 25, the radiation patterns at both frequencies.

Based on the results obtained it is clear that the air gap between the MWR and the GPS L1 antennas, reduced the efficiency in the L1 band, and the AR increased, tending to a linear polarization instead of a circular or elliptical.

In the end, the FM of the nadir antenna is not compliant with all the requirements. Unfortunately, due to the schedule of the mission and the required delivery date, it was not feasible time-wise to perform another iteration. Despite this, antenna imperfections were characterized, included in the retrieval algorithms, allowing to successfully retrieve soil moisture [42], sea ice concentration and extent [23,43], thickness [22], and sea salinity [44].

5. Conclusions

This study has presented the design for the implementation and tests of the flight model of a dual-frequency left-hand circular polarization patch antenna array, including a 6:1 combiner. The design has to comply with functional, performance, and environmental requirements. It has flown in the $^3Cat-5/A$ satellite, from the FSSCat mission.

The nadir antenna has been designed to fit in an envelope of $300 \times 200 \times 7$ mm^3. For that reason, it is conformed by four PCBs, with a thickness of 1.52 mm. The dielectric used is Rogers 4003C. Based on the dimensions of the envelope and the directivity requirements the design solution has been to implement a dual-band six-patch array with a stripline combiner.

The design of the antennas has been an iterative process of simulating, prototyping, and then, adjusting the central frequencies. During the different iterations performed two aspects of the antennas were identified: (1) the matching frequency is dependent on the dimensions of the patches, so manufacturing tolerances affect the matching of the antenna, and (2) the tolerance in the dielectric constant of the material also affects the matching of the antenna. Moreover, there is a difference between the central frequencies obtained in the simulations and the prototypes.

In the iterative process, the first two single frequency elements with LHCP were prototyped, to characterize the material and verify the simulation model. Then, a dual-band with LHCP antenna was designed. From this design, the Flight Model antenna was manufactured, being the same antenna but in a six elements array configuration.

The 6:1 ports combiner was also simulated and prototyped. The simulations have a constant isolation parameter for the MWR band of

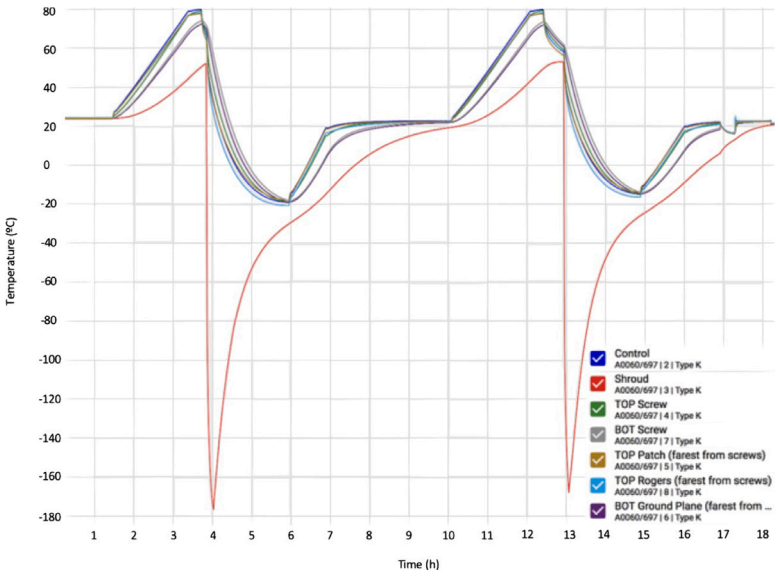

Fig. 22. Temperature readings from thermocouples during TVAC test.

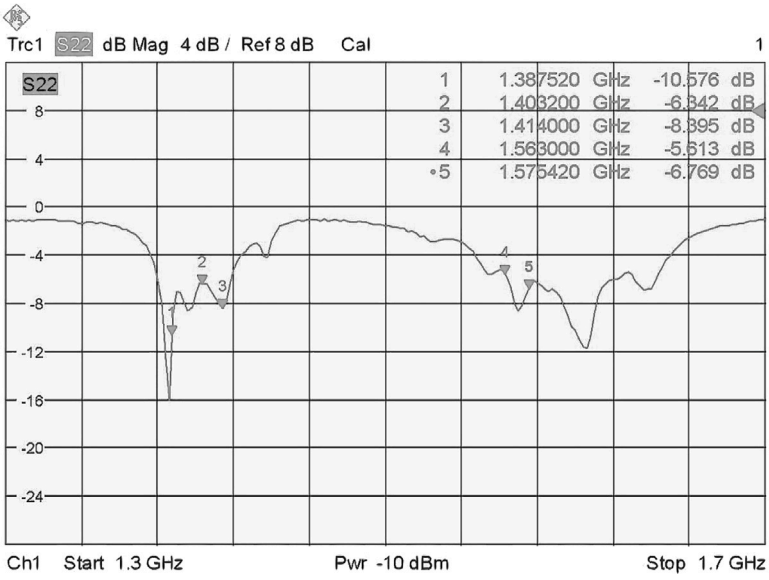

Fig. 23. S11 Parameter results for the nadir antenna FM.

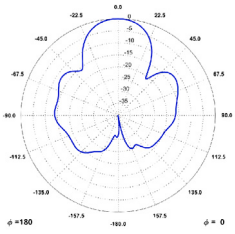

(a) 3U direction

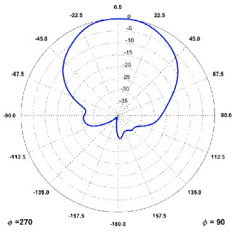

(b) 2U direction

Fig. 24. Radiation patterns measured at 1413 MHz of the nadir antenna FM.

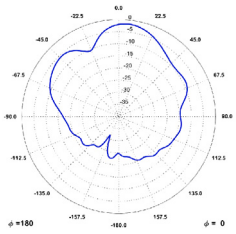

(a) 3U direction

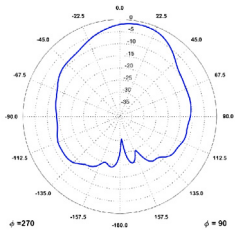

(b) 2U direction

Fig. 25. Radiation patterns measured at 1575.42 MHz of the nadir antenna FM.

approximately −8.0 dB. This is not the case for the prototype, probably because the interface holes of the antenna do not have uniform distribution and may affect the striplines.

The nadir antenna FM was manufactured following the exact dimensions of the prototypes. However, during the assembly process, the resonance for the 1575.42 MHz was at a higher frequency, so an air gap existed between the MWR band radiating elements and the L1 ones.

The antenna was tested in a TVAC, to verify that the performance does not vary in space conditions, performing two thermal cycles between +80 °C and −20 °C. After that, the radiation performance was measured concluding that the GPS L1 results were not all compliant with the requirements, although the MWR band did comply in terms of the Directivity and Axial Ratio. In orbit scientific products of both the MWR, and the GNSS-R payloads were obtained. However, in the case of GNSS-R, only those signals with high Signal-to-Noise Ratios (SNRs) were received due to the lower directivity of the antenna. For future missions, it would be optimum to remanufacture an antenna which complies with all the stated requirements.

CRediT authorship contribution statement

Lara Fernandez: Conceptualization, Methodology, Software, Validation, Formal analysis, Investigation, Data curation, Writing of this study. **Joan Francesc Munoz-Martin:** Methodology, Validation, Review of this study. **Joan A. Ruiz-de-Azua:** Methodology, Validation, Review of this study. **Anna Calveras:** Conceptualization, Review of this study. **Adriano Camps:** Conceptualization, Resources, Supervision, Project administration, Funding acquisition, Review of this study.

Declaration of competing interest

The authors declare that they have no known competing financial interests or personal relationships that could have appeared to influence the work reported in this paper.

References

[1] Mr Heidt, Prof Puig-suari, Prof Augustus, S Moore, Prof Nakasuka, Prof Robert, J Twiggs, CubeSat: A new generation of picosatellite for education and industry low-cost space experimentation, in: USU Conference on Small Satellites, 2000.

[2] Cal Poly, CubeSat design specification, 2022, Accessed: September 2022. URL https://www.cubesat.org/s/CDS-REV14_1-2022-02-09.pdf.

[3] NASA, Icecube, 2022, Accessed: September 2022. URL https://atmospheres.gsfc.nasa.gov/climate/index.php?section=259.

[4] JPL, Radar in a CubeSat (RainCube), 2022, Accessed: September 2022. URL https://www.jpl.nasa.gov/cubesat/missions/raincube.php.

[5] M.P. Clarizia, Christopher Ruf, Wind Speed Retrieval Algorithm for the Cyclone Global Navigation Satellite System (CYGNSS) Mission, IEEE Trans. Geosci. Remote Sens. (2016) 1–14, http://dx.doi.org/10.1109/TGRS.2016.2541343.

[6] Adriano Camps, Hyuk Park, Miriam Pablos, Giuseppe Foti, Christine Gommenginger, Pang-Wei Liu, Jasmeet Judge, Sensitivity of GNSS-r spaceborne observations to soil moisture and vegetation, IEEE J. Sel. Top. Appl. Earth Obs. Remote Sens. 9 (2016) 1–13, http://dx.doi.org/10.1109/JSTARS.2016.2588467.

[7] C. Chew, John Reager, Eric Small, CYGNSS data map flood inundation during the 2017 Atlantic hurricane season, Sci. Rep. 8 (2018) http://dx.doi.org/10.1038/s41598-018-27673-x.

[8] A. Alonso-Arroyo, V.U. Zavorotny, A. Camps, Sea ice detection using U.K. TDS-1 GNSS-R data, IEEE Trans. Geosci. Remote Sens. (ISSN: 1558-0644) 55 (9) (2017) 4989–5001, http://dx.doi.org/10.1109/TGRS.2017.2699122.

[9] eoPortal Directory, UK-DMC-2, 2022, Accessed: September 2022. URL https://directory.eoportal.org/web/eoportal/satellite-missions/u/uk-dmc-2.

[10] ESA, TechDemoSat-1 (Technology Demonstration Satellite-1) / TDS-1, 2021, Accessed: September 2022. URL https://earth.esa.int/web/eoportal/satellite-missions/t/techdemosat-1.

[11] NASA, Cygnss, 2022, Accessed: September 2022. URL https://www.nasa.gov/cygnss.

[12] H.M.J.P. Barre, B. Duesmann, Y.H. Kerr, SMOS: The mission and the system, IEEE Trans. Geosci. Remote Sens. 46 (3) (2008) 587–593, http://dx.doi.org/10.1109/TGRS.2008.916264.

[13] D. Entekhabi, E.G. Njoku, P.E. O'Neill, K.H. Kellogg, W.T. Crow, W.N. Edelstein, J.K. Entin, S.D. Goodman, T.J. Jackson, J. Johnson, J. Kimball, J.R. Piepmeier, R.D. Koster, N. Martin, K.C. McDonald, M. Moghaddam, S. Moran, R. Reichle, J.C. Shi, M.W. Spencer, S.W. Thurman, L. Tsang, J. Van Zyl, The soil moisture active passive (SMAP) mission, Proc. IEEE 98 (5) (2010) 704–716, http://dx.doi.org/10.1109/JPROC.2010.2043918.

[14] E. Valencia, A. Camps, N. Rodriguez-Alvarez, I. Ramos-Perez, X. Bosch-Lluis, H. Park, Improving the accuracy of sea surface salinity retrieval using GNSS-r data to correct the sea state effect, Radio Science 46 (06) (2011) 1–11, http://dx.doi.org/10.1029/2011RS004688.

[15] A. Camps, A. Golkar, A. Gutierrez, J. A. R. de Azua, J.F. Munoz-Martin, L. Fernandez, C. Diez, A. Aguilella, S. Briatore, R. Akhtyamov, N. Garzaniti, Fsscat, the 2017 copernicus masters' "esa sentinel small satellite challenge" winner: A federated polar and soil moisture tandem mission based on 6U cubesats, in: IGARSS 2018 - 2018 IEEE International Geoscience and Remote Sensing Symposium, 2018, pp. 8285–8287, http://dx.doi.org/10.1109/IGARSS.2018.8518405.

[16] Copernicus Masters, FSSCat - towards federated EO systems, 2022, Accessed: September 2022. URL https://www.copernicus-masters.com/winner/ffscat-towards-federated-eo-systems/.

[17] J.F. Munoz-Martin, L. Fernandez, A. Perez, H. Park, J. Ruiz-de Azua, A. Camps, In-orbit validation of the FMPL-2 dual microwave payload onboard the fsscat mission, in: 2021 IEEE International Geoscience and Remote Sensing Symposium IGARSS, 2021, pp. 7884–7887, http://dx.doi.org/10.1109/IGARSS47720.2021.9554298.

[18] Isaac Ramos-Perez, Adriano Camps, Xavi Bosch-Lluis, Nereida Rodriguez-Alvarez, Enric Valencia-Domènech, Hyuk Park, Giuseppe Forte, Merce Vall-llosera, PAU-SA: A synthetic aperture interferometric radiometer test bed for potential improvements in future missions, Sensors (ISSN: 1424-8220) 12 (6) (2012) 7738–7777, http://dx.doi.org/10.3390/s120607738.

[19] H. Carreno-Luengo, A. Camps, I. Perez-Ramos, G. Forte, R. Onrubia, R. Díez, 3Cat-2: A p(y) and c/a GNSS-r experimental nano-satellite mission, in: 2013 IEEE International Geoscience and Remote Sensing Symposium - IGARSS, 2013, pp. 843–846, http://dx.doi.org/10.1109/IGARSS.2013.6721290.

[20] J.F. Munoz-Martin, N. Miguelez, R. Castella, L. Fernandez, A. Solanellas, P. Via, A. Camps, 3Cat-4: Combined GNSS-r, L-band radiometer with RFI mitigation, and AIS receiver for a I-Unit cubesat based on software defined radio, in: IGARSS 2018 - 2018 IEEE International Geoscience and Remote Sensing Symposium, 2018, pp. 1063–1066, http://dx.doi.org/10.1109/IGARSS.2018.8519037.

[21] ESA, First earth observation satellite with ai ready for launch, 2022, Accessed: September 2022. URL http://www.esa.int/Our_Activities/Observing_the_Earth/First_Earth_observation_satellite_with_AI_ready_for_launch/(print).

[22] Christoph Herbert, Joan Francesc Munoz-Martin, David Llaveria, Miriam Pablos, Adriano Camps, Sea ice thickness estimation based on regression neural networks using L-band microwave radiometry data from the FSSCat mission, Remote Sens. (ISSN: 2072-4292) 13 (7) (2021) http://dx.doi.org/10.3390/rs13071366.

[23] David Llaveria, Juan Francesc Munoz-Martin, Christoph Herbert, Miriam Pablos, Hyuk Park, Adriano Camps, Sea ice concentration and sea ice extent mapping with L-band microwave radiometry and GNSS-R data from the FFSCat mission using neural networks, Remote Sens. (ISSN: 2072-4292) 13 (6) (2021) http://dx.doi.org/10.3390/rs13061139.

[24] Suhila Abulgasem, Faisel Tubbal, Raad Raad, Panagiotis Ioannis Theoharis, Sining Lu, Saeid Iranmanesh, Antenna designs for CubeSats: A review, IEEE Access 9 (2021) 45289–45324, http://dx.doi.org/10.1109/ACCESS.2021.3066632.

[25] Lars Alminde, Karl Kaas, Morten Bisgaard, Johan Christiansen, David Gerhardt, AIAA small satellites conference, in: GOMX-1 Flight Experience and Air Traffic Monitoring Results, AIAA, 2014.

[26] David Gerhardt, Morten Bisgaard, Lars Alminde, Roger Walker, Miguel Angel Fernandez, Anis Latiri, Jean-Luc Issler, AIAA small satellites conference, in: GOMX-3: Mission Results from the Inaugural ESA in-Orbit Demonstration CubeSat, AIAA, 2016.

[27] Lacuna Space, Lacuna, 2022, Accessed: September 2022. URL https://www.lacuna.space/.

[28] Helical Communication Technologies, Helios deployable antenna, 2022, Accessed: September 2022. URL https://www.helicomtech.com/helios-deployable-antenna.

[29] Lara Fernandez, Marco Sobrino, Joan Adria Ruiz-de Azua, Anna Calveras, Adriano Camps, Design of a deployable helix antenna at L-band for a 1-unit CubeSat: From theoretical analysis to flight model results, Sensors (ISSN: 1424-8220) 22 (10) (2022).

[30] Lara Fernandez, Marco Sobrino, Oriol Milian, Andrea Aguilella, Arnau Solanellas, Marc Badia, Joan Francesc Munoz-Martin, Joan Adria Ruiz de Azua, Miquel Sureda, Adriano Camps, Deployment mechanism for a L-band helix antenna in 1-unit cubesat, Acta Astronaut. (ISSN: 0094-5765) (2020) http://dx.doi.org/10.1016/j.actaastro.2020.09.005.

[31] H. Carreno-Luengo, A. Camps, P. Via, J.F. Munoz, A. Cortiella, D. Vidal, J. Jané, N. Catarino, M. Hagenfeldt, P. Palomo, S. Cornara, 3Cat-2—An experimental nanosatellite for GNSS-R earth observation: Mission concept and analysis, IEEE J. Sel. Top. Appl. Earth Obs. Remote Sens. (ISSN: 2151-1535) 9 (10) (2016) 4540–4551, http://dx.doi.org/10.1109/JSTARS.2016.2574717.

[32] Mohammad Alibakhshikenari, Bal S. Virdee, Leyre Azpilicueta, Mohammad Naser-Moghadasi, Mobayode Olusola Akinsolu, Chan Hwang See, Bo Liu, Raed A. Abd-Alhameed, Francisco Falcone, Isabelle Huynen, Tayeb A. Denidni, Ernesto Limiti, A comprehensive survey of "Metamaterial transmission-line based antennas: Design, challenges, and applications", IEEE Access 8 (2020) 144778–144808, http://dx.doi.org/10.1109/ACCESS.2020.3013698.

[33] Mohammad Alibakhshikenari, Fatemeh Babaeian, Bal S. Virdee, Sonia Aïssa, Leyre Azpilicueta, Chan Hwang See, Ayman Abdulhadi Althuwayb, Isabelle Huynen, Raed A. Abd-Alhameed, Francisco Falcone, Ernesto Limiti, A comprehensive survey on "Various decoupling mechanisms with focus on metamaterial and metasurface principles applicable to SAR and MIMO antenna systems", IEEE Access 8 (2020) 192965–193004, http://dx.doi.org/10.1109/ACCESS.2020.3032826.

[34] Constantine A. Balanis, Antenna Theory: Analysis and Design, John wiley & sons, 2016.

[35] Stefano Maci, G. Biffi Gentili, Dual-frequency patch antennas, IEEE Antennas Propag. Mag. 39 (6) (1997) 13–20.

[36] Miaomiao Zuo, Jian Ren, Rongxu Hou, Xiaoyu Du, Zhe Chen, Y.-Z Yin, Compact dual-band antenna with large frequency ratio, AEU - Int. J. Electron. Commun. 141 (2021) 153978, http://dx.doi.org/10.1016/j.aeue.2021.153978.

[37] Chun Xu Mao, Steven Gao, Yi Wang, Benito Sanz-Izquierdo, Zhengpeng Wang, Fan Qin, Qing Xin Chu, Jianzhou Li, Gao Wei, Jiadong Xu, Dual-band patch antenna with filtering performance and harmonic suppression, IEEE Trans. Antennas and Propagation 64 (9) (2016) 4074–4077, http://dx.doi.org/10.1109/TAP.2016.2574883.

[38] Wing Chi Mok, Sai Hoi Wong, Kwai Man Luk, Kai Fong Lee, Single-layer single-patch dual-band and triple-band patch antennas, IEEE Trans. Antennas and Propagation 61 (8) (2013) 4341–4344, http://dx.doi.org/10.1109/TAP.2013.2260516.

[39] Wenwei Wang, Chunhong Chen, Shiyan Wang, Wen Wu, Switchable dual-band dual-sense circularly polarized patch antenna implemented by dual-band phase shifter of ±90°, IEEE Trans. Antennas and Propagation 69 (10) (2021) 6912–6917, http://dx.doi.org/10.1109/TAP.2021.3070055.

[40] Universitat Politècnica de Catalunya - BarcelonaTech, Anechoic chamber, 2022, Accessed: September 2022. URL https://www.tsc.upc.edu/en/facilities/anechoic-chamber.

[41] Universitat Politècnica de Catalunya - BarcelonaTech, Facilities - NanoSat lab, 2022, Accessed: September 2022. URL https://nanosatlab.upc.edu/en/facilities-folder.

[42] J.F. Munoz-Martin, D. Llavería, C. Herbert, M. Pablos, A. Camps, Soil moisture retrieval using the FMPL-2/FSSCat GNSS-r and microwave radiometry data, in: 2021 IEEE International Geoscience and Remote Sensing Symposium IGARSS, 2021, pp. 7638–7641, http://dx.doi.org/10.1109/IGARSS47720.2021.9553438.

[43] David Llaveria, Juan Francesc Munoz-Martin, Christoph Herbert, Miriam Pablos, Adriano Camps, Hyuk Park, Sea ice concentration and sea ice extent mapping with the fsscat mission: A neural network approach, in: 2021 IEEE International Geoscience and Remote Sensing Symposium IGARSS, 2021, pp. 7823–7826, http://dx.doi.org/10.1109/IGARSS47720.2021.9554793.

[44] Joan Francesc Munoz-Martin, Adriano Camps, Sea surface salinity and wind speed retrievals using GNSS-r and L-band microwave radiometry data from FMPL-2 onboard the fsscat mission, Remote Sens. (ISSN: 2072-4292) 13 (16) (2021) http://dx.doi.org/10.3390/rs13163224.